

www.acsaem.org Article

Synergistic Integration of LLZAO-Based Hybrid Membrane and Quasi-Solid Electrolyte for High-Performance and Thermally Stable Lithium-Ion Batteries

Ji-Wan Kim, Heesu Kim, Jusung Song, Seungmo Koo, Yong-Wook Kim, Hyeonjae Roh, and Dong-Won Kim*



Cite This: ACS Appl. Energy Mater. 2025, 8, 15427-15437



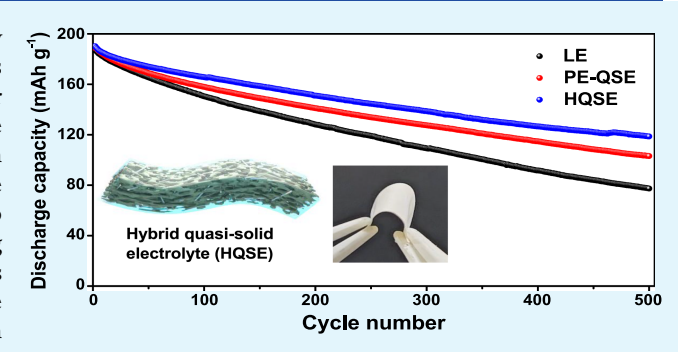
ACCESS I

III Metrics & More

Article Recommendations

s Supporting Information

ABSTRACT: Lithium-ion batteries (LIBs) have been extensively used in various energy storage systems, such as mobile electronics and electric vehicles. However, the growing demand for higher energy density and improved safety necessitates alternative electrolyte systems to replace conventional liquid electrolytes. In this work, we prepared a hybrid quasi-solid-state electrolyte (HQSE) incorporating a Li⁺-conducting oxide electrolyte. To fabricate the HQSE, a porous hybrid membrane was formed using poly(vinylidene fluoride-*co*-hexafluoropropylene) and fibrous Li_{6.4}La₃Zr₂Al_{0.2}O₁₂ (LLZAO) via a phase-inversion method. The hybrid membrane was then impregnated with a precursor solution containing liquid electrolyte and cross-linking agent, followed by



thermal curing to finally obtain the HQSE. The resulting HQSE exhibited excellent oxidative stability, high ionic conductivity, high Li⁺ transference number, nonflammability, and enhanced thermal stability. The graphite/LiNi_{0.8}Co_{0.1}Mn_{0.1}O₂ cell employing the HQSE delivered a high initial capacity of 188.8 mAh g⁻¹ at 0.5C and 25 °C, along with excellent capacity retention of 85.2% at 25 °C and 62.4% at 55 °C after 500 cycles, outperforming the cell with liquid electrolyte. Our results demonstrate that the developed HQSE offers a promising alternative to conventional liquid electrolytes, enabling high performance and enhanced safety in LIBs.

KEYWORDS: hybrid quasi-solid electrolyte, porous hybrid membrane, Li⁺-conductive oxide electrolyte, lithium-ion batteries, enhanced safety

■ INTRODUCTION

Lithium-ion batteries (LIBs) have been widely adopted as the primary energy storage system for mobile electronics due to their high energy density and long cycle life. With the growing use of LIBs in electric vehicles and large-scale energy storage systems, there is an increasing demand for next-generation batteries with even higher energy density, longer cycle life, and enhanced safety. 1-3 One of the most effective strategies to improve energy density is the use of nickel-rich layered oxide cathodes, such as LiNi_xCo_yMn_{1-x-y}O₂ (NCM, $x \ge 0.8$), which offer high capacity and operating voltage.4,5 However, conventional liquid electrolytes suffer from limited oxidative stability, leading to anodic decomposition at high voltages. This decomposition increases internal resistance and accelerates capacity fading during cycling.^{6,7} In addition, the flammability of liquid electrolytes raises serious safety concerns in LIBs.8,9

To address these limitations, quasi-solid-state electrolytes (QSEs) have been investigated as alternatives to liquid electrolytes due to their enhanced safety and improved cycling performance. However, their inherently low ionic con-

ductivity remains a critical drawback, limiting rate capability of the cell. Moreover, although QSEs are known to reduce flammability by immobilizing organic solvents within the polymer matrix, the cells using QSEs are still flammable due to the potential ignition of the polyolefin separator and liquid components. In contrast, solid electrolytes have emerged as promising alternatives to address the aforementioned challenges. Among them, oxide-based inorganic electrolytes, particularly garnet-type Li₇La₃Zr₂O₁₂ (LLZO), have attracted considerable attention owing to their relatively high ionic conductivity, wide electrochemical stability window, and nonflammability. Despite these advantages, oxide electrolytes suffer from high interfacial resistance, poor mechanical flexibility and thin film formability, which hinder their practical

Received: August 12, 2025
Revised: September 30, 2025
Accepted: October 10, 2025
Published: October 14, 2025





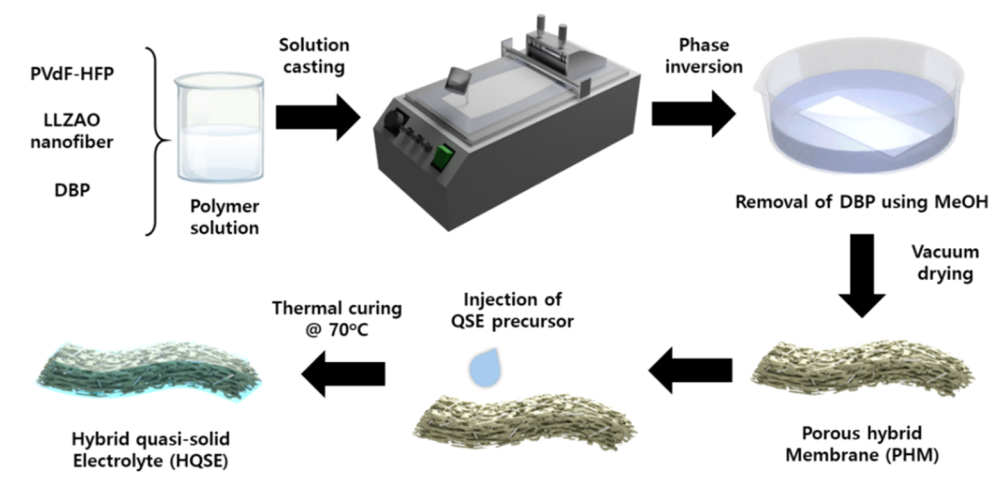


Figure 1. Schematic illustration for the preparation process of the HQSE.

application. 16,17 Therefore, integrating oxide electrolytes with flexible QSEs offers an effective strategy for developing high-performance and safe electrolytes by compensating for the limitations of each component. 18-21

In this study, we prepared the hybrid quasi-solid-state electrolytes (HQSEs) that combine the mechanical robustness and high ionic conductivity of oxide electrolytes with the flexibility and interfacial stability of QSEs. The porous hybrid membrane, composed of Li_{6.4}La₃Zr₂Al_{0.2}O₁₂ (LLZAO) nanofibers embedded within poly(vinylidene fluoride-co-hexafluoropropylene) (PVdF-HFP) matrix, serves as a mechanically robust and ionically conductive framework. In these HQSEs, the fibrous morphology of LLZAO provides continuous Li⁺ion conduction pathways that enable efficient ion transport, unlike particle-type LLZAO, which suffer from large grain boundary resistance that hinders ion movement. We selected PVdF-HFP because of its superior mechanical robustness, electrochemical stability, and proven ability to form porous hybrid membrane with inorganic oxides. Moreover, PVdF-HFP exhibits greater moisture resistance compared with poly(ethylene oxide)(PEO), thereby offering improved stability within the battery system. The porous hybrid membrane is then impregnated with a precursor solution containing liquid electrolyte and cross-linking agent, followed by thermal curing to form the hybrid quasi-solid-state electrolyte (HQSE). The resulting HQSE exhibited high ionic conductivity, high Li+ transference number, and excellent electrochemical stability. Furthermore, the use of the HQSE effectively suppressed thermal shrinkage of the electrolyte at elevated temperatures (160 °C) and exhibited nonflammability, thereby enhancing the battery safety. The graphite/ LiNi_{0.8}Co_{0.1}Mn_{0.1}O₂ (NCM, active mass: 15.0 mg cm⁻²) cell incorporating the HQSE was evaluated under both roomtemperature and elevated-temperature conditions. It delivered a high initial discharge capacity of 188.8 mAh g⁻¹ at 25 °C and 0.5C, and demonstrated outstanding cycling stability, retaining 85.2% of its initial capacity at 25 °C and 62.4% at 55 °C after 500 cycles, which surpass the cycling performance of liquid electrolyte counterpart.

EXPERIMENTAL SECTION

Materials. Lithium nitrate (LiNO₃), lanthanum(III) nitrate hexahydrate (La(NO₃)₃·6H₂O), zirconium acetate (Zr(CH₃COO)₄), poly(vinylpyrrolidone) (PVP, M_w : 1,300,000), dibutyl phthalate (DBP), and trimethylolpropane trimethacrylate (TMPTMA) were

purchased from Sigma-Aldrich. Aluminum nitrate nonahydrate $(Al(NO_3)_3 \cdot 9H_2O)$ and 2-2' azobis(2-methylpropionitrile) (AIBN) were supplied by Junsei and TCI, respectively. Poly(vinylidene fluoride-co-hexafluoropropylene) (PVdF-HFP, M_w : 470,000) was obtained from Arkema. The liquid electrolyte used in this study consisted of 1.15 M LiPF $_6$ dissolved in a mixed solvent of ethylene carbonate, ethyl methyl carbonate, and diethyl carbonate in a 3:5:2 volume ratio, with 5 wt % fluoroethylene carbonate as an additive. It was kindly provided by Dongwha Electrolyte.

Fabrication of Porous Hybrid Membrane. A porous hybrid membrane (PHM) was prepared using Li_{6.4}La₃Zr₂Al_{0.2}O₁₂ (LLZAO) nanofibers and PVdF-HFP via solution casting and phase inversion methods. First, the LLZAO nanofibers were synthesized through electrospinning, subsequent sintering and calcination, as shown in Figure S1a.^{22,23} The electrospinning solution consisted of appropriate amounts of LiNO₃, La(NO₃)₃·₆H₂O, Al(NO₃)₃·9H₂O, and PVP, dissolved in a mixture of zirconium acetate and acetic acid. The electrospun membrane was then sintered and calcined at 750 °C for 4 h, during which the organic components were completely removed. Figures S1b and S1c show the electrospun PVP membrane and the synthesized LLZAO nanofibers. The diameter of the resulting LLZAO fibers was less than 500 nm, and the BET surface area was measured to be 3.24 m² g⁻¹. To fabricate the PHM, PVdF-HFP (0.25 g) was dissolved in acetone (4.0 mL), and LLZAO nanofibers (1.0 g) along with DBP (0.3 g) were added to the solution. The resulting mixture was ball-milled for 24 h to ensure homogeneous dispersion of the nanofibers in the polymer solution. The mixture was then cast onto a polypropylene film using a doctor blade and dried in an oven at 40 °C to remove the acetone solvent. After drying, the resulting membrane was immersed in methanol to create pores by extracting the DBP, followed by drying in a vacuum oven at 80 °C for 24 h.

Preparation of the Lithium-Ion Cell. QSE precursor was prepared by adding 4.0 wt % TMPTMA and a trace amount of AIBN to the liquid electrolyte. The cathode was fabricated by casting a slurry composed of NCM (L&F Co., Ltd.), Super P (TIMCAL), and poly(vinylidene fluoride) (PVdF, Solef 5130, Solvay) in a weight ratio of 95:3:2, using N-methyl-2-pyrrolidone (NMP, Sigma-Aldrich) as the solvent, onto an aluminum (Al) current collector. The anode was similarly prepared via a slurry-casting method on a copper (Cu) foil, using a slurry consisting of artificial graphite (S360, BTR), PVdF and Super P (91:8:1 by weight) in NMP. The active material loadings in the fabricated NCM and graphite electrodes were 15.0 and 10.1 mg cm⁻², respectively. A 2032 coin-type cell was assembled in an Ar-filled glovebox (MBRAUN) under high-purity argon atmosphere, using the prepared anode and cathode along with the PHM or polyethylene (PE) separator. The QSE precursor was then injected into the cell, followed by thermal curing at 70 °C for 2 h to form the HQSE or PE-QSE by in situ polymerization of the precursor.

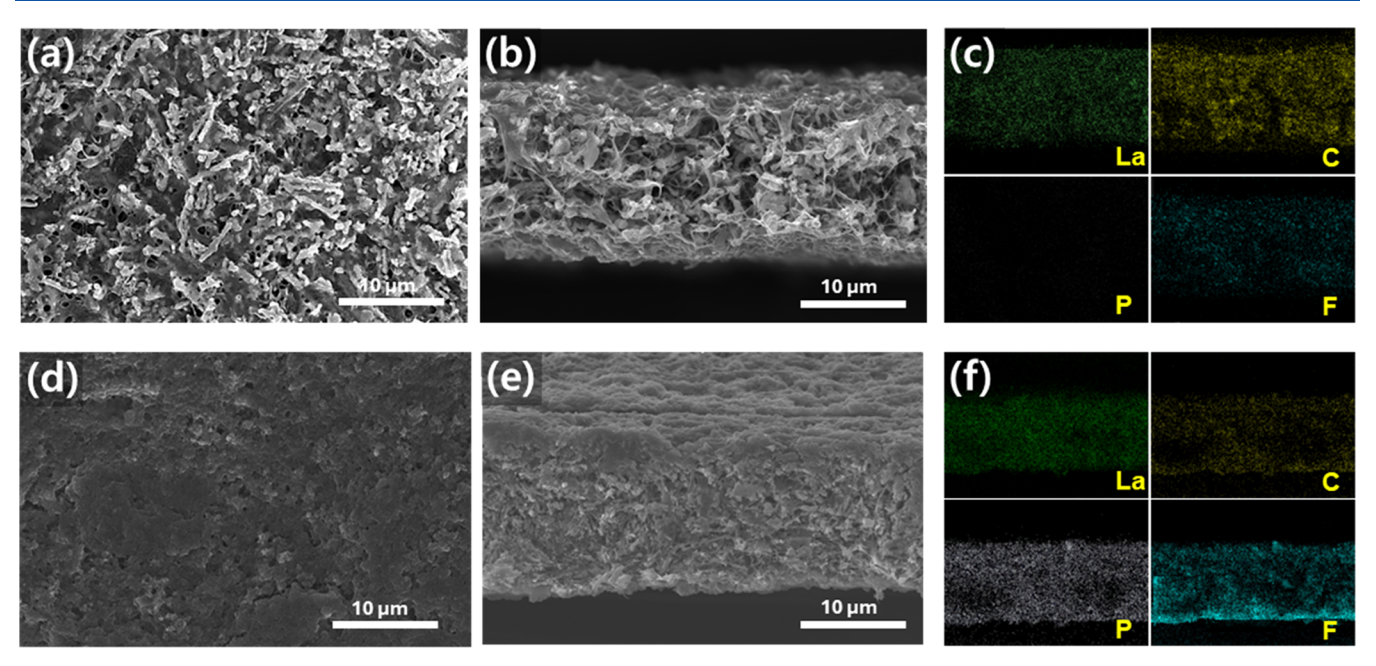


Figure 2. FE-SEM and EDS mapping images of PHM and HQSE. (a) Surface and (b) cross-sectional SEM images of the PHM, and (c) its elemental maps. (d) Surface and (e) cross-sectional SEM images of the HQSE, and (f) its elemental maps.

Characterization and Measurements. Fourier-transform infrared (FT-IR) spectra were recorded in the range of 400-4000 cm using a Nicolet iS50 spectrometer. The morphology of the PHM was examined using field-emission scanning electron microscopy (FE-SEM; Verios G4) equipped with energy-dispersive X-ray spectroscopy (EDS). X-ray diffraction (XRD; D8 Advance, Bruker) was performed to investigate the crystalline structure of the synthesized LLZAO nanofibers, PVdF-HFP, and PHM in the 2θ range of $10-80^{\circ}$. To investigate the thermal properties of HQSE, differential scanning calorimetry (DSC, TA Instruments) was conducted at a heating rate of 10 °C min⁻¹. Thermogravimetric analysis (TGA, STA 449 F3, Netzsch) of HQSE was performed in the temperature range of 25-700 °C at 10 °C min⁻¹. Mechanical properties were evaluated via nanoindentation using a NanoTest NTX device (Micro Materials) under a load of 10 mN. The chemical compositions of the cathode electrolyte interphase (CEI) formed on the cathode surface were analyzed by X-ray photoelectron spectroscopy (XPS; Thermo Fisher) using an Al K α source. All XPS spectra were calibrated to the hydrocarbon peak at a binding energy of 284.9 eV. In addition, ⁷Li solid-state magic angle spinning (MAS) NMR spectra of the HQSE were recorded using a Bruker 400 MHz NMR spectrometer at a spinning rate of 10 kHz. Electrochemical impedance spectroscopy (EIS) was performed over a frequency range of 0.1 Hz to 1 MHz with an amplitude of 10 mV using a CHI660d analyzer (CH Instruments). Linear sweep voltammetry was conducted to evaluate the electrochemical stability of the electrolyte at a scan rate of 1.0 mV s⁻¹. Leakage current was measured in the graphite/NCM cell at 4.3 V after three formation cycles. Cycling tests of the graphite/NCM cell were carried out in the voltage range of 2.5-4.3 V using a battery tester (WBCS3000, WonATech Co., Ltd.) at both 25 and 55 °C.

■ RESULTS AND DISCUSSION

Figure 1 presents a schematic illustration for the preparation process of the HQSE. A PHM was fabricated using LLZAO nanofibers and PVdF-HFP via solution casting and phase-inversion methods. After solution casting, the residual DBP in the membrane was extracted during the phase-inversion process using methanol, thereby generating pores within the PHM. The QSE precursor containing TMPTMA was then infiltrated into the PHM and in situ polymerized at 70 °C for 2 h, resulting in the formation of the HQSE. Fibrous LLZAO

was used in the preparation of the PHM, because its fiber-like morphology provides higher ionic conductivity compared to powder-type LLZAO, thereby enhancing both the ionic conductivity and mechanical strength of the HQSE. ^{25,26}

The optimal weight ratio of LLZAO in the PHM was determined by comparing the ionic conductivities and mechanical properties of the prepared HQSEs. As shown in Figure S2a, the HQSE exhibited the highest ionic conductivity at 90 wt % LLZAO, attributed to the facile formation of Li⁺ ion conduction pathways. However, at such a high LLZAO composition, the HQSE was very brittle and difficult to fabricate into a flexible film (Figure S2c). Therefore, 80 wt % LLZAO was selected as the optimal composition, considering both ionic conductivity and mechanical flexibility (Figure S2b). The thickness of the HQSE was measured to be 24 μ m using a micrometer (Figure S2d). The formation of the QSE from the precursor was confirmed by the optical images shown in Figure S3a. After thermal curing of the QSE precursor at 70 °C for 2 h, a nonfluidic QSE was obtained. To verify the polymerization of TMPTMA in the precursor, FT-IR analysis was conducted, and the results are presented in Figure S3b. The peaks associated with C=O bonds between 1700 and 1800 cm⁻¹ indicate that the carbonate solvents and TMPTMA were incorporated into the HQSE. The disappearance of the C=C double bond peak at 1650 cm⁻¹ after thermal curing confirms the successful polymerization of TMPTMA.²⁶

Figure 2a—c present the surface and cross-sectional SEM images of the PHM, along with its EDX mapping results. The PHM exhibited a porous structure, and the fibrous LLZAO was well embedded within the membrane, providing continuous Li⁺ ion conduction pathways. The porosity of the PHM was measured using *n*-butanol, as previously reported.^{27,28} The PHM exhibited a porosity of 54.6%, which is higher than that of PE separator (39.8%). The elemental maps show that La, C, and F are uniformly distributed, indicating a homogeneous dispersion of LLZAO within the PVdF-HFP based PHM. Figure 2d—e display the SEM images of the HQSE obtained after thermal curing of the QSE

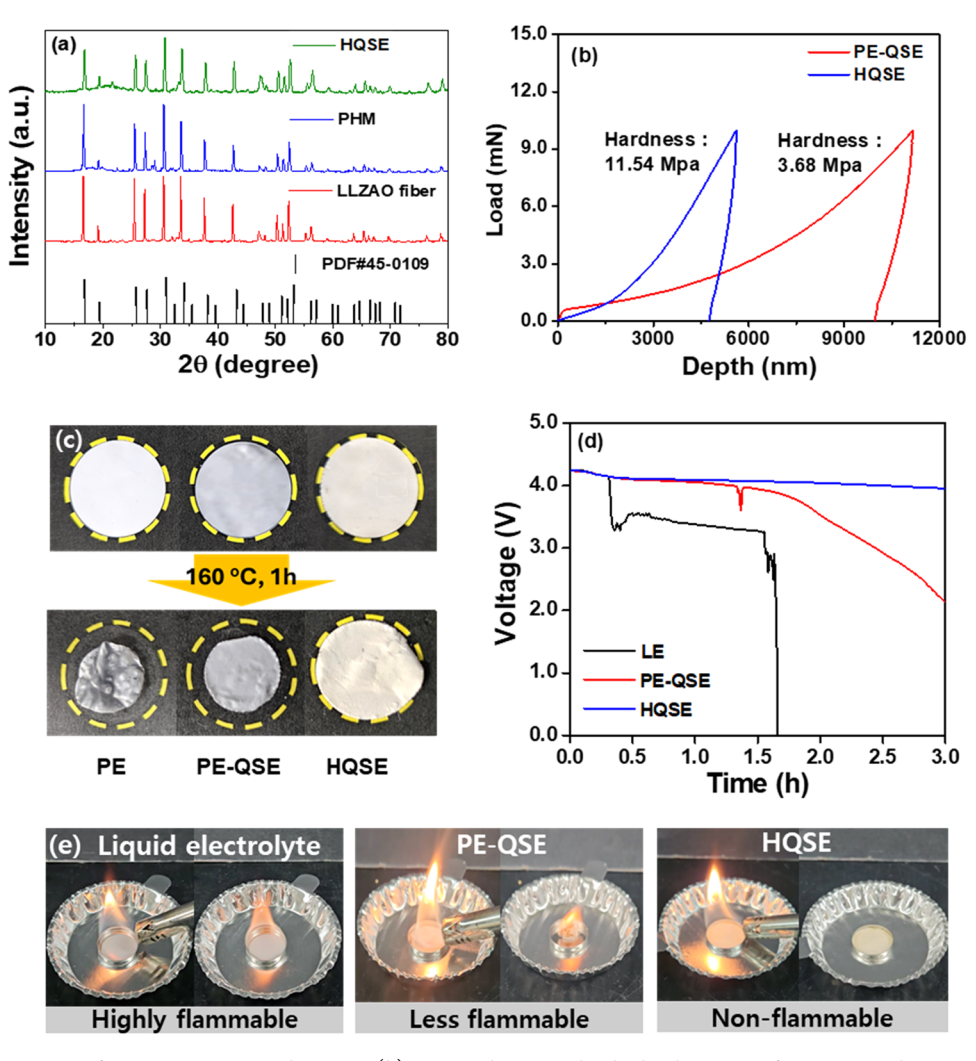


Figure 3. (a) XRD patterns of LLZAO, PHM, and HQSE. (b) Nanoindentation load—depth curves of PE-QSE and HQSE. (c) Optical images showing the thermal shrinkage of PE, PE-QSE, and HQSE before and after heating at 160 °C for 1 h. (d) Variation in the open-circuit voltage of cells with different electrolytes during storage at 160 °C for 3 h. (e) Flammability comparison of the liquid electrolyte, PE-QSE, and HQSE.

precursor. Both the surface and cross-sectional images reveal that the pores in the PHM were filled with the QSE, resulting in a dense morphology. The EDS mapping images in Figure 2f demonstrate the uniform presence of the phosphorus element from the ${\rm LiPF}_6$ salt within the HQSE, indicating a homogeneous distribution of the QSE throughout the HQSE.

Figure 3a presents the XRD patterns of LLZAO nanofibers, PHM, and HQSE. The crystalline peaks of the LLZAO nanofibers are consistent with those of pure cubic-phase Li₇La₃Zr₂O₁₂ (PDF #45-0109), confirming the successful synthesis of cubic-phase LLZAO nanofibers. The XRD patterns of the PHM and HQSE retain the characteristic crystalline peaks of LLZAO nanofibers, indicating that the LLZAO nanofibers remain chemically stable with solvent and PVdF-HFP, and that the incorporation of the QSE exerts negligible influence on the crystalline structure of LLZAO. In the XRD patterns of PVdF-HFP and QSE (Figure S4a), pristine PVdF-HFP displayed distinct crystalline peaks, whereas the QSE exhibited a fully amorphous pattern. The disappearance of the PVdF-HFP crystalline peaks in HQSE is attributed to the penetration of the liquid electrolyte into the polymer matrix, which disrupts the strong intermolecular interactions and ordered chain packing of PVdF-HFP. In addition, the filler effect of LLZAO nanofibers further destroys

the crystalline domains of PVdF-HFP. 29 As shown in the DSC thermograms (Figure S4b), consistent with the XRD results, no crystalline peaks of the polymer were observed in HQSE. The solid content of HQSE was determined by TGA analysis (Figure S5). HQSE retained about 60 wt % of its initial mass at 350 °C. Based on these results, the liquid electrolyte content was calculated to be 40 wt % (36 wt % organic solvents and 4 wt % LiPF₆). The liquid electrolyte in HQSE contributes additional ionic conduction while being immobilized within the cross-linked matrix and PHM. The mechanical properties of the HQSE were compared with those of the QSE-infiltrated PE separator (PE-QSE). A nanoindentation test was performed to evaluate the mechanical properties of the HQSE and PE-QSE under a maximum load of 10 mN. As the load increased, the nanoindenter tip gradually penetrated the surface of the electrolyte, with harder materials showing shallower penetration depths. As shown in Figure 3b, the HQSE exhibited a lower penetration depth and higher hardness than the PE-QSE, which is attributed to the presence of rigid LLZAO nanofibers in the HQSE. The hardness values of the PE-QSE and HQSE were measured to be 3.68 and 11.54 MPa, respectively, demonstrating that the incorporation of QSE into the LLZAO-based PHM significantly enhanced the mechanical strength of the HQSE. 30,31 Figure 3c presents

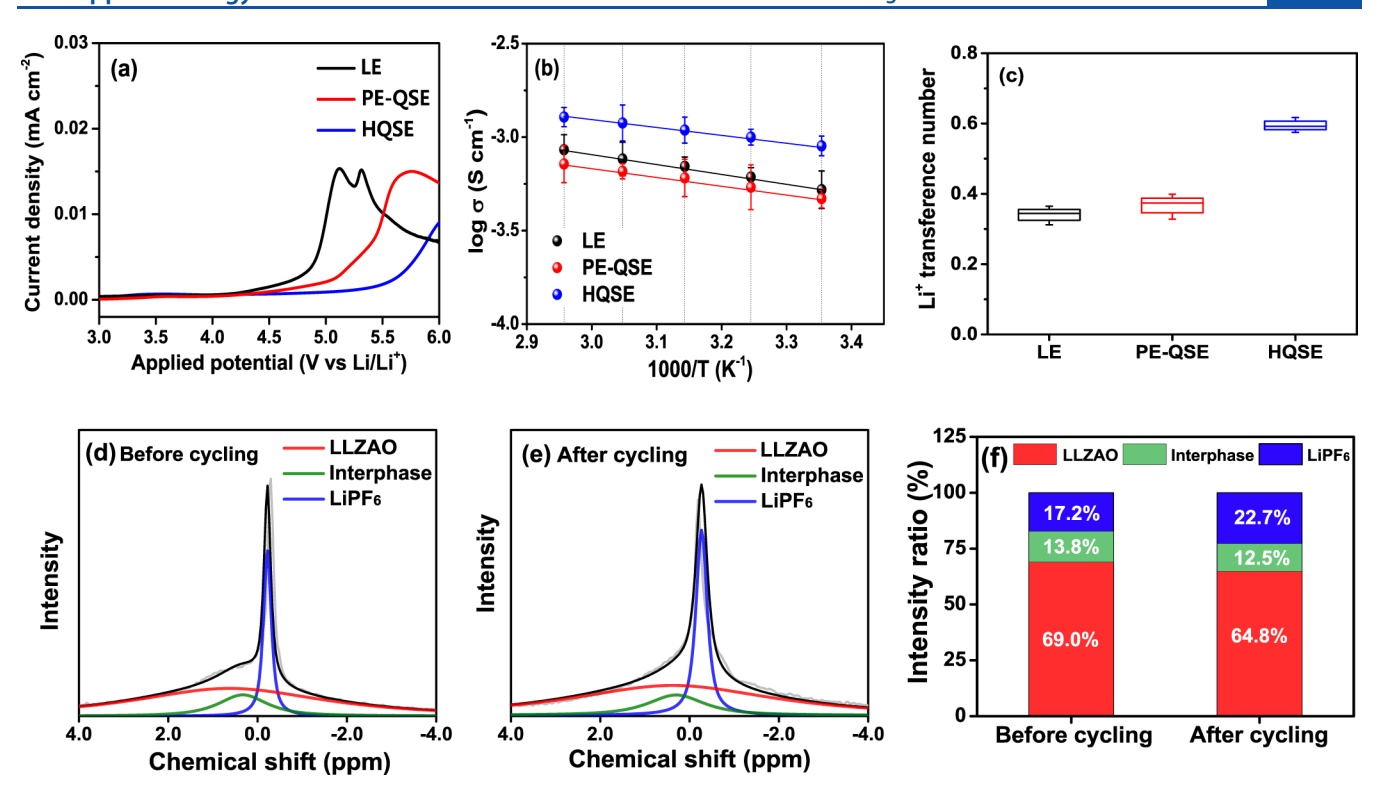


Figure 4. (a) Linear sweep voltammetry curves, (b) ionic conductivities, and (c) Li⁺ transference numbers of different electrolytes. Solid-state MAS ⁷Li NMR spectra of HQSE (d) before and (e) after galvanostatic cycling of the ⁶Li/HQSE/⁶Li cell. (f) Peak intensity ratios of each ⁷Li component in the NMR spectra.

optical images of the PE, PE-QSE, and HQSE before and after storage at 160 °C for 1 h. The PE separator exhibited significant thermal shrinkage, whereas the PE-QSE mitigated this shrinkage due to the presence of a cross-linked polymer network. Notably, the HQSE showed no visible shrinkage even after high-temperature storage, confirming its superior thermal stability. The thermal stability of the lithium-ion (graphite/ NCM) cell was evaluated by monitoring the open-circuit voltage (OCV) of the fully charged cell at 160 °C for 3 h. As shown in Figure 3d, the OCV of the cell with liquid electrolyte dropped to 0 V after 1.65 h, indicating an internal short-circuit between the anode and cathode. In contrast, the PE-QSE cell exhibited improved voltage stability, attributed to the enhanced dimensional stability provided by the cross-linked polymer network. Notably, the HQSE cell maintained a stable OCV under high-temperature conditions, demonstrating that the superior thermal stability of HQSE effectively prevented internal short-circuiting at elevated temperatures. A flammability test was conducted to compare the flame retardancy of different electrolytes by exposing them to a flame source. As shown in Figure 3e, the liquid electrolyte ignited immediately due to its high flammability and burned violently. In the case of the PE-QSE (Figures 3e and S6), it did not ignite during brief exposure but eventually caught fire after prolonged exposure. This is because the cross-linked polymer network in the QSE helps immobilize flammable solvents, however flammable components such as the PE separator can still cause ignition. In contrast, the HQSE remained completely nonflammable even under prolonged exposure, owing to the presence of nonflammable LLZAO.

Linear sweep voltammetry was conducted to evaluate the electrochemical stability of the electrolytes. In the cathodic scan (Figure S7), no additional peaks were observed in PE-

QSE and HQSE compared to the liquid electrolyte, indicating that the cross-linked network, PVdF-HFP, and LLZAO fibers do not affect the reductive stability of HQSE. In Figure 4a, oxidative decomposition of the liquid electrolyte occurred at approximately 4.5 V vs Li/Li⁺, which increased to 4.7 V for the PE-QSE. The improved oxidative stability is attributed to the encapsulation of the liquid electrolyte, which reduces its direct contact with the electrodes. In the case of HQSE, the onset potential further increased to 5.5 V, owing to the high oxidative stability of the LLZAO fillers. 32,33 The leakage current test further supports these results, showing that the HQSE cell exhibited the lowest leakage current at 4.3 V (Figure S8). Figure 4b presents the ionic conductivities of the liquid electrolyte, PE-QSE, and HQSE. To evaluate the ionic conductivity under practical cell conditions, the conductivity of the liquid electrolyte was measured after soaking PE separator with the liquid electrolyte. Notably, the HQSE exhibited the highest ionic conductivity across all temperatures. This result is attributed to the high ionic conductivity of the LLZAO nanofibers in the HQSE, whereas the conventional PE separator hindered ion transport.³⁴ To demonstrate the effect of fibrous LLZAO on ionic conductivity, a porous hybrid membrane incorporating powder-type LLZAO ($d_{50} = 500 \text{ nm}$) was also prepared using the same fabrication process. As shown in Figure S9, the HQSE containing fibrous LLZAO exhibited higher ionic conductivity at room temperature compared to the HQSE with powder-type LLZAO. This is because the fibrous LLZAO provides more continuous Li⁺ conduction pathways than powder-based LLZAO particles, and its large surface area creates a broader interphase with QSE, which is known to serve as an Li+ transport pathway in hybrid electrolytes. 24,35 The Li⁺ transference numbers of the electrolytes were determined using the Bruce-Vincent method, based

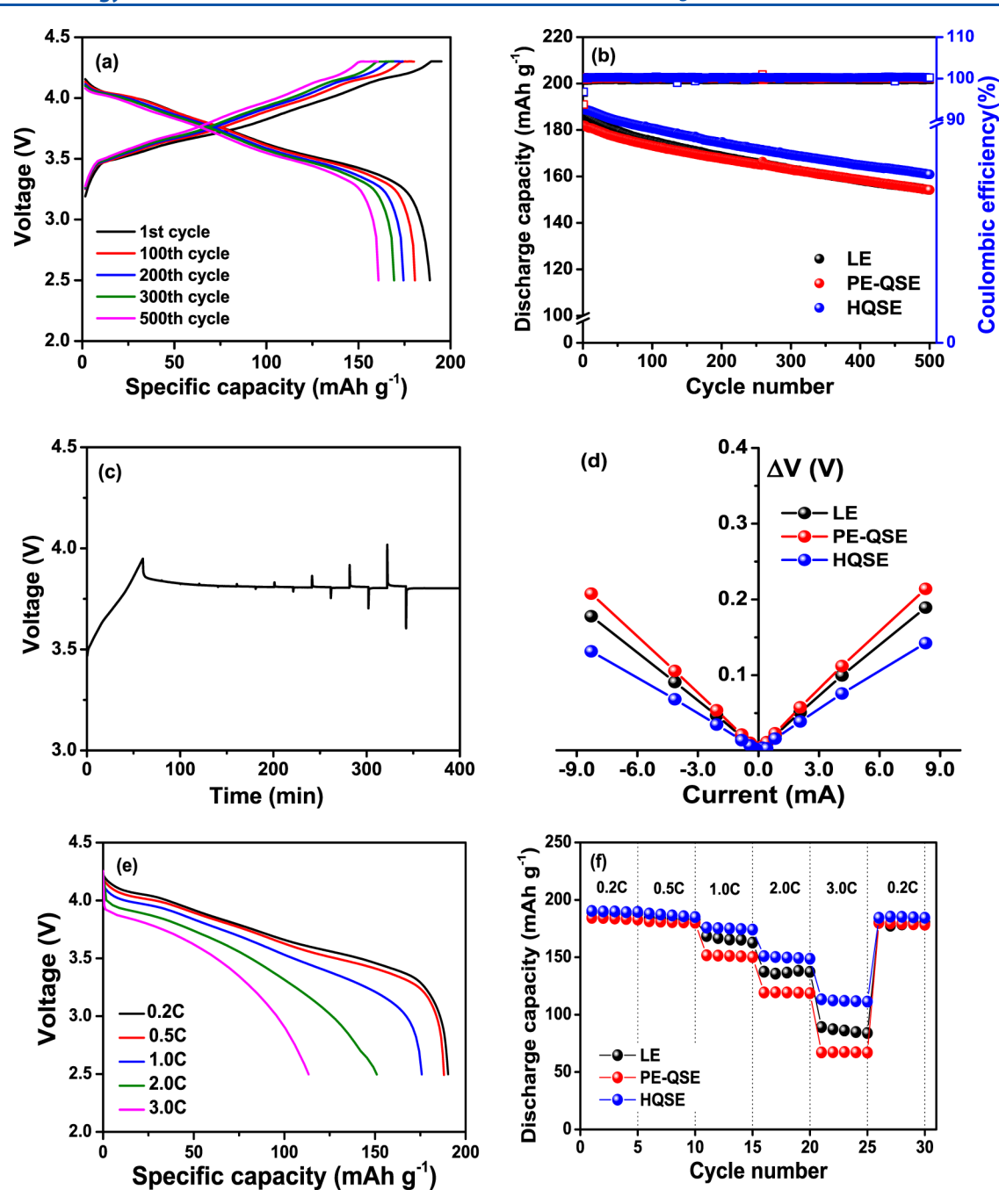


Figure 5. (a) Voltage curves of the cell employing HQSE and (b) cycling performance of the cells with different electrolytes at 0.5C and 25 °C. (c) Voltage response of the cell with HQSE, and (d) plots of the voltage change vs current rate in the cells with various electrolytes during DC-IR test. (e) Discharge curves of the cell with HQSE at different C rates, and (f) discharge capacities of the cells with different electrolytes as a function of C rate.

on dc polarization and EIS analysis.³⁶ Figure S10 shows the AC impedance spectra and dc polarization results of the Li symmetric cell with HQSE. The calculated Li⁺ transference numbers for the different electrolytes are presented in Figure 4c. The HQSE exhibited the highest Li⁺ transference number of 0.59, while the liquid electrolyte and PE-QSE showed values of 0.34 and 0.37, respectively. The increased Li⁺ transference number in HQSE is mainly attributed to the single-ion conduction behavior of the LLZAO nanofibers. The Li⁺ ion conduction pathway in HQSE was investigated using ⁷Li solid-state MAS NMR.^{31,37} The cycling curves of the ⁶Li symmetric cell with HQSE are shown in Figure S11, demonstrating stable

cycling behavior (Li stripping and deposition) at a constant current density of 0.2 mA cm $^{-2}$ with charge of 0.2 mAh cm $^{-2}$ for each cycle. This performance is superior to that of the symmetric cell with liquid electrolyte, which exhibited a gradual increase in overpotential after 25 cycles. The 7 Li NMR spectra of HQSE before and after galvanostatic cycling of the symmetric 6 Li/ 6 Li cell are shown in Figure 4d,e, respectively. According to previous reports, the sharp peak at -0.21 ppm corresponds to LiPF $_6$ salt in the QSE, while the broad peak at 0.7 ppm is attributed to LLZAO. 38 The peak observed at 0.3 ppm is assigned to the interphase of LLZAO, which is known to play a key role in Li $^+$ ion conduction. 39,40 During cycling,

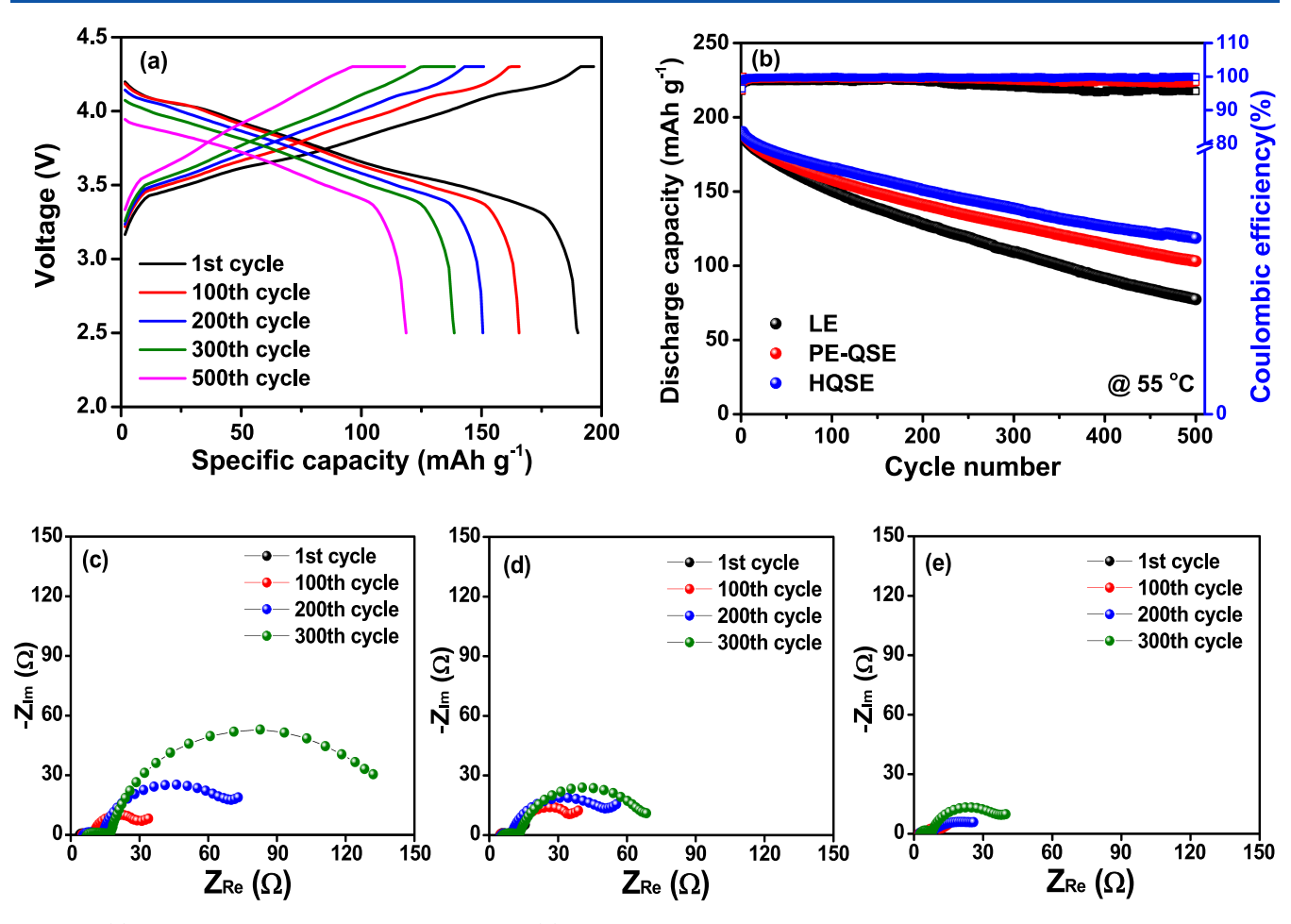


Figure 6. (a) Voltage curves of the cell with HQSE and (b) cycling stability of cells employing various electrolytes at 0.5C and 55 °C. AC impedance spectra of the cells with (c) liquid electrolyte, (d) PE-QSE, and (e) HQSE at 55 °C.

⁶Li⁺ ions oxidized at the ⁶Li electrode migrate to the opposite electrode through the electrolyte, leading to the partial substitution of ⁷Li⁺ ions in the electrolyte with ⁶Li⁺ ions. As a result, the proportion of ⁷Li⁺ ions in the electrolyte gradually decreases with continued cycling. The intensity ratios of the different ⁷Li peaks are presented in Figure 4f, showing that the ⁷Li content in the LLZAO nanofibers and their interphase decreased, while the proportion of ⁷Li in the LiPF₆ component in the QSE increased. This result indicates that LLZAO and its interphase primarily facilitate Li⁺ ion transport rather than the QSE, contributing to the high ionic conductivity of HQSE. Based on the above results, the Li⁺ ion conduction pathways within HQSE can be schematically illustrated, as shown in Figure S12.

The cycling behavior of graphite/NCM cells using various electrolytes was assessed at 25 °C. All cells were precycled at 0.1C rate for two cycles and subsequently cycled at 0.5C and same temperature. The voltage profiles of the cells are shown in Figures 5a and S13, and their cycling performances are compared in Figure 5b. The cell employing HQSE delivered a high initial discharge capacity of 188.8 mAh g⁻¹ at 0.5C, which was higher than those of the cells using liquid electrolyte or PE-QSE. Moreover, the HQSE cell exhibited good capacity retention of 85.2% after 500 cycles at 0.5C rate and 25 °C. The internal resistance of the cells was determined using direct current internal resistance (DC-IR) measurements at 25 °C. The DC-IR test was conducted at 50% state of charge and

current rate of 0.1C, with applied current rates of 0.025C, 0.05C, 0.1C, 0.2C, 0.5C, 1.0C, and 2.0C. Figure 5c shows the voltage profiles of the cell with HQSE during the DC-IR experiments, and Figure 5d presents the voltage changes at different current densities, where the linear slope of each plot corresponds to the internal resistance of the cell. The internal resistance of the HOSE cell was lower than those of the cells with other electrolytes, which is attributed to the enhanced ionic conductivity of the HQSE. The rate capability of the cells was evaluated at 25 °C, and the resulting voltage profiles at different C rates are shown in Figure 5e. During the test, the charging rate was fixed at 0.2C, while the discharging rate was varied from 0.2C to 0.5C, 1.0C, 2.0C, and 3.0C, then returned to 0.2C. As shown in Figure 5f, the cell with HQSE exhibited the highest discharge capacities at all C-rates, consistent with the DC-IR results indicating the lowest internal resistance.

We also fabricated a bicell pouch cell with dimension of 4.0 × 5.0 cm². As shown in Figure S14, the pouch cell initially delivered a discharge capacity of 120 mAh and retained 88.6% of its capacity after 300 cycles at 1.0C and 25 °C. These results demonstrate that HQSE can be successfully scaled up to pouch-cell operation while maintaining comparable performance trends.

The high temperature cycling stability of the cells was evaluated. The voltage profiles of the cells at 55 $^{\circ}$ C are shown in Figures 6a and S15. When the temperature increased, the initial discharge capacities of the cells slightly increased compared to those at 25 $^{\circ}$ C. As depicted in Figure 6b, the

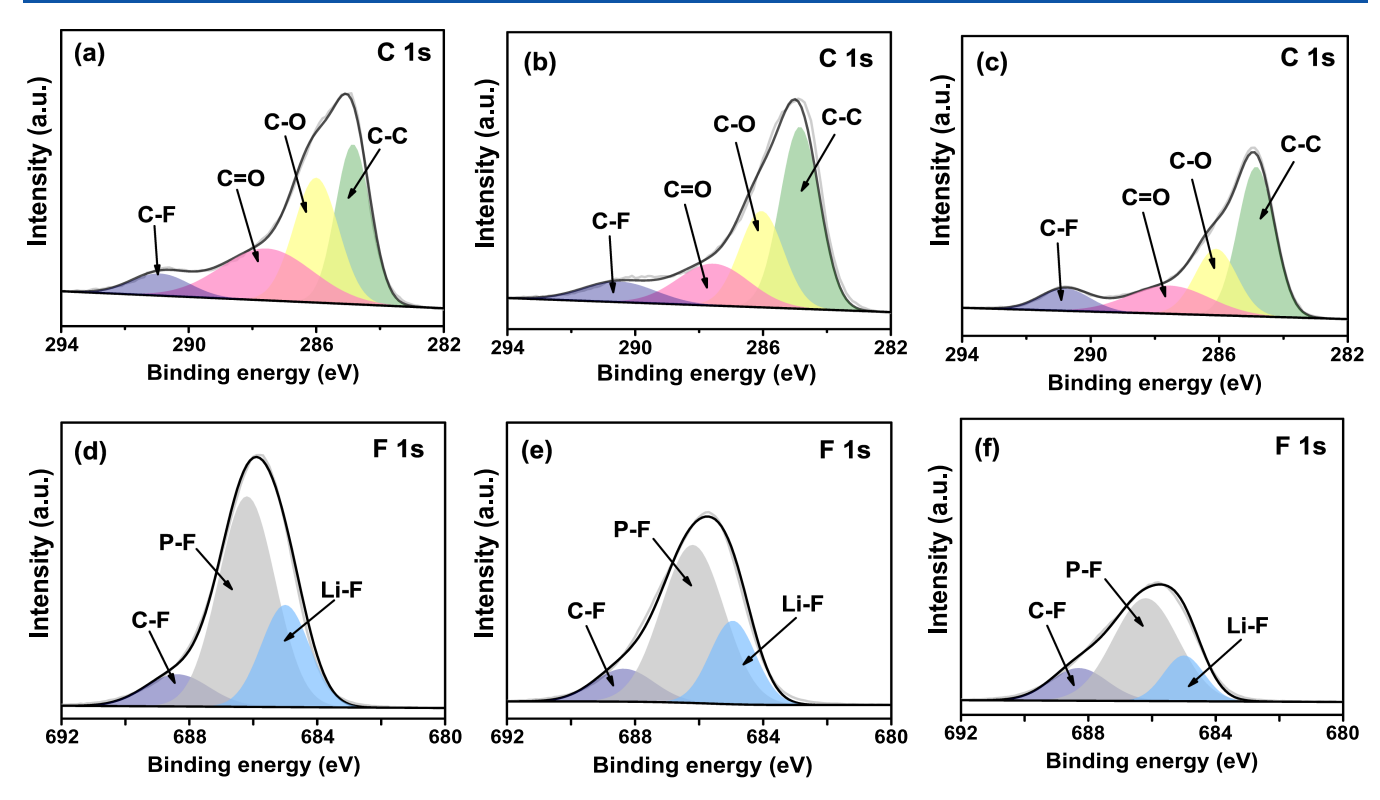


Figure 7. C 1s XPS spectra of the cathodes cycled in (a) liquid electrolyte, (b) PE-QSE, and (c) HQSE at 55 °C. F 1s XPS spectra of the cathodes cycled in (d) liquid electrolyte, (e) PE-QSE, and (f) HQSE at 55 °C.

HQSE cell exhibited the best cycling stability among all the cells at elevated temperature. Notably, the liquid electrolyte cell showed a gradual decline in Coulombic efficiency during cycling, resulting in low Coulombic efficiency of 95.7% at the 500th cycle, which was significantly lower than that of the HOSE cell (99.9%). This result indicates that the cell with the liquid electrolyte underwent side reactions at high temperature, leading to significant capacity fading. The cycling performances of the cells employing different electrolytes at 25 and 55 °C are compared in the same figure (Figure S16). It is evident that the cell with HQSE exhibited the best cycling stability at both temperatures. A comparative table summarizing the ionic conductivity, Li⁺ transference number, oxidative stability, and cycling performance of cells employing different quasi-solidstate electrolytes reported to date is presented in Table S1 to contextualize the advancement of our study. It reveals that the HQSE developed in this work exhibits superior electrochemical characteristics and cycling performance.

To investigate the resistance variations during cycling at 55 °C, EIS analysis was performed every 100 cycles up to the 300th cycle, and the results are shown in Figure 6c-e. The spectra were fitted using an equivalent circuit in Figure S17. It is well-known that the first x-intercept corresponds to the bulk resistance of electrolyte (R_h) , while the depressed semicircle in the midfrequency region represents resistance related to the anode side (R_a) and the semicircle in the low-frequency region corresponds to cathode side (R_c) . The R_a is associated with the graphite degradation and the growth of nonuniform SEI, while R_c reveals the formation of CEI and cathode degradation. The variations in fitted resistance of the cells with different electrolytes are shown in Figure S18. As shown in the figures, the cell with HQSE exhibited the lowest resistance at every cycle. As cycling progressed, all the cells showed an increase in resistance, with a particularly pronounced increase in R_c . This

significant rise in R_c is primarily attributed to the formation of unstable CEI from electrolyte decomposition, and the degradation caused by the HF generated from the thermal decomposition of LiPF₆ at elevated temperatures. 44 Among the cells, the liquid electrolyte cell exhibited the largest increase in internal resistance, whereas the HOSE cell showed the smallest change. This result is attributed to the superior chemical and electrochemical stability of the HQSE at elevated temperatures, which helps mitigate the degradation of the cell. Furthermore, oxide-based inorganic materials are known to scavenge small amounts of HF, which accelerates cell degradation. Thus, the HF-scavenging effect of LLZAO likely contributes to suppressing the increase in resistance.⁴⁵ The cross-sectional SEM images of the cathodes after 100 cycles are shown in Figure S19. The NCM cathode cycled with liquid electrolyte exhibited larger volume expansion and more microcracks within the active material compared to the cathode cycled with HQSE, indicating that HQSE effectively suppressed side reactions and preserved the structural stability of the cathode active materials during repeated cycling.⁴

Figure 7 presents the XPS spectra of the NCM cathodes cycled in different electrolytes. The analysis was conducted at charged state after 300 cycles at 55 °C. The C 1s XPS spectra mainly reflect organic components resulting from the decomposition of organic solvents, while the F 1s spectra provide information about salt decomposition. In the C 1s spectra (Figure 7a-c), the peaks corresponding to C-O, C=O, and C-F were observed at 286.1, 287.5, and 290.8 eV, respectively. The relative intensity of the C-F peak, which originates from the PVdF binder in the cathode, was used as an internal reference. Compared to the C-F peak, the intensities of the C=O and C-O peaks were significantly higher in the liquid electrolyte cell, indicating extensive thermal and oxidative decomposition of the organic solvents during

high-temperature cycling. In contrast, these peaks were notably reduced in the PE-QSE and HQSE cells, suggesting suppressed solvent decomposition. In the F 1s spectra (Figure 7d-f), three characteristic peaks were identified at 688.3 eV (C-F), 686.2 eV (P-F), and 684.9 eV (Li-F). 49 Among these, the P-F and Li-F peaks are attributed to the decomposition of LiPF₆ salt, whereas the C-F peak is derived from the PVdF binder. Notably, the intensities of the P-F and Li-F peaks were markedly higher in the liquid electrolyte cell than in the PE-QSE and HQSE cells, indicating more severe salt decomposition in the liquid electrolyte system. In contrast, the HQSE cell exhibited the lowest intensities for these peaks, confirming that HQSE effectively suppressed both organic solvent and lithium salt decomposition at the cathode, thereby contributing to superior cycling stability at elevated temperatures. Similar results were observed for the graphite anode after cycling (Figure S20). In particular, the intensities of the C=O and C-O peaks in the C 1s spectra and the P-F peak in the F 1s spectra were remarkably reduced when HQSE was used, confirming the suppression of electrolyte decomposition at the graphite anode.

CONCLUSIONS

In this study, HQSE was prepared by integrating quasi-solid electrolyte (QSE) with a porous hybrid membrane containing LLZAO nanofibers and PVdF-HFP. The QSE precursor, composed of liquid electrolyte and small amount of crosslinker, was injected into the porous hybrid membrane and subsequently thermally cured to form a cross-linked polymer network within the Li⁺-conductive porous membrane. The resulting HOSE exhibited high ionic conductivity, improved oxidative stability, and enhanced thermal stability due to the synergistic combination of the LLZAO-based hybrid membrane and the quasi-solid electrolyte. Compared to the liquid electrolyte and PE-QSE cells, the HQSE cell showed a higher discharge capacity, superior cycling stability and rate performance at room temperature. Moreover, its cycling stability at 55 °C was significantly improved relative to those of the liquid electrolyte and PE-QSE cells. Our results demonstrate that the integration of the LLZAO-based hybrid membrane with the quasi-solid electrolyte effectively complements each component's properties, enabling high-performance LIBs with excellent cycling stability and enhanced thermal safety.

ASSOCIATED CONTENT

Supporting Information

The Supporting Information is available free of charge at https://pubs.acs.org/doi/10.1021/acsaem.5c02528.

Schematic illustration for the fabrication process of LLZAO nanofibers, SEM images of electrospun PVP-based polymer nanofibers and LLZAO nanofibers; Ionic conductivities of HQSEs, Optical images and thickness measurement of the HQSE; Optical images of the QSE, FT-IR spectra of the PHM and HQSEs before and after thermal curing; XRD patterns and DSC thermograms; TGA curve of HQSE; Flammability test results of PE-QSE; LSV curves of different electrolytes in the cathodic scan; Leakage current of cells with different electrolytes at 4.3 V and 25 °C; Ionic conductivities of the liquid electrolyte, PE-QSE, and HQSEs; AC impedance spectra of Li/HQSE/Li cell and dc polarization current curves; Voltage profiles of the symmetric 6Li/liquid electro-

lyte/⁶Li and ⁶Li/HQSE/⁶Li cells; Schematic illustration of the Li⁺ ion conduction pathways within HQSE; Voltage profiles of the graphite/NCM cells with liquid electrolyte and PE-QSE at 0.5C and 25 °C; Voltage profiles and cycling performance of the pouch-type bicell; Voltage profiles of the graphite/NCM cells with liquid electrolyte and PE-QSE at 0.5C and 55 °C; cycling performance of the cells with LE, PE-QSE, and HQSE at 25 and 55 °C; comparison of electrochemical properties and cycling performance of the cells with different quasi-solid-state electrolytes; The equivalent circuit for AC impedance results; The fitted values of resistance of the cells; Cross-sectional SEM images of cycled cathodes; C 1s and F 1s XPS spectra of the graphite anodes cycled at 55 °C (PDF)

AUTHOR INFORMATION

Corresponding Author

Dong-Won Kim — Department of Chemical Engineering, Hanyang University, Seoul 04763, Republic of Korea; Department of Battery Engineering, Hanyang University, Seoul 04763, Republic of Korea; orcid.org/0000-0002-1735-0272; Phone: +82222202337;

Email: dongwonkim@hanyang.ac.kr.; Fax: +82222984101

Authors

Ji-Wan Kim – Department of Chemical Engineering, Hanyang University, Seoul 04763, Republic of Korea

Heesu Kim – Department of Chemical Engineering, Hanyang University, Seoul 04763, Republic of Korea

Jusung Song – Department of Chemical Engineering, Hanyang University, Seoul 04763, Republic of Korea

Seungmo Koo – Department of Battery Engineering, Hanyang University, Seoul 04763, Republic of Korea

Yong-Wook Kim – Fundamental Materials Technology Team, Doosan Corporation, Gyeonggi-do 16858, Republic of Korea Hyeonjae Roh – Fundamental Materials Technology Team, Doosan Corporation, Gyeonggi-do 16858, Republic of Korea

Complete contact information is available at: https://pubs.acs.org/10.1021/acsaem.5c02528

Notes

The authors declare no competing financial interest.

ACKNOWLEDGMENTS

This work was supported by the Doosan Corporation and the National Research Foundation of Korea funded by the Korean government (RS-2024-00454354).

REFERENCES

- (1) Armand, M.; Tarascon, J.-M. Building Better Batteries. *Nature* **2008**, *451*, 652–657.
- (2) Etacheri, V.; Marom, R.; Elazari, R.; Salitra, G.; Aurbach, D. Challenges in the Development of Advanced Li-Ion Batteries: A Review. *Energy Environ. Sci.* **2011**, *4*, 3243–3262.
- (3) Goodenough, J. B.; Park, K.-S. The Li-Ion Rechargeable Battery: A Perspective. J. Am. Chem. Soc. 2013, 135, 1167–1176.
- (4) Myung, S.-T.; Maglia, F.; Park, K.-J.; Yoon, C. S.; Lamp, P.; Kim, S.-J.; Sun, Y.-K. Nickel-Rich Layered Cathode Materials for Automotive Lithium-Ion Batteries: Achievements and Perspectives. ACS Energy Lett. 2017, 2, 196–223.
- (5) Kim, J.-H.; Park, K.-J.; Kim, S. J.; Yoon, C. S.; Sun, Y.-K. A Method of Increasing the Energy Density of Layered Ni-Rich

- $Li[Ni_{1-2x}Co_xMn_x]O_2$ Cathodes (x = 0.05, 0.1, 0.2). *J. Mater. Chem. A* **2019**, 7, 2694–2701.
- (6) Kondo, Y.; Abe, T.; Yamada, Y. Kinetics of Interfacial Ion Transfer in Lithium-Ion Batteries: Mechanism Understanding and Improvement Strategies. ACS Appl. Mater. Interfaces 2022, 14, 22706–22718.
- (7) Kim, J.; Adiraju, V. A. K.; Rodrigo, N.; Hoffmann, J.; Payne, M.; Lucht, B. L. Lithium Bis(trimethylsilyl) Phosphate as a Novel Bifunctional Additive for High-Voltage LiNi₁₋₅Mn₀₋₅O₄/Graphite Lithium-Ion Batteries. *ACS Appl. Mater. Interfaces* **2021**, 13, 22351–22360.
- (8) Chen, Y.; Kang, Y.; Zhao, Y.; Wang, L.; Liu, J.; Li, Y.; Liang, Z.; He, X.; Li, X.; Tavajohi, N.; Li, B. A Review of Lithium-Ion Battery Safety Concerns: The Issues, Strategies, and Testing Standards. *J. Energy Chem.* **2021**, *59*, 83–99.
- (9) Jeevarajan, J. A.; Joshi, T.; Parhizi, M.; Rauhala, T.; Juarez-Robles, D. Battery Hazards for Large Energy Storage Systems. *ACS Energy Lett.* **2022**, *7*, 2725–2733.
- (10) Park, S.; Jeong, B.; Lim, D.-A.; Lee, C. H.; Ahn, K. H.; Lee, J. H.; Kim, D.-W. Quasi-Solid-State Electrolyte Synthesized Using a Thiol—Ene Click Chemistry for Rechargeable Lithium Metal Batteries with Enhanced Safety. ACS Appl. Mater. Interfaces 2020, 12, 19553—19562.
- (11) Hao, Q.; Yan, J.; Gao, Y.; Chen, F.; Chen, X.; Qi, Y.; Li, N. In Situ Formed Gel Polymer Electrolytes Enable Stable Solid Electrolyte Interface for High-Performance Lithium Metal Batteries. *ACS Appl. Mater. Interfaces* **2024**, *16*, 44689–44696.
- (12) Li, X.; Li, Z.; Zhang, W.; Jiang, X.; Han, L.; Wang, X.; Kan, Y.; Song, L.; Hu, Y. Flame-Retardant In-Situ Formed Gel Polymer Electrolyte with Different Valance States of Phosphorus Structures for High-Performance and Fire-Safety Lithium-Ion Batteries. *Chem. Eng. J.* 2024, 490, No. 151568.
- (13) Han, L.; Liao, C.; Liu, Y.; Yu, H.; Zhang, S.; Zhu, Y.; Li, Z.; Li, X.; Kan, Y.; Hu, Y. Non-Flammable Sandwich-Structured TPU Gel Polymer Electrolyte without Flame Retardant Addition for High Performance Lithium-Ion Batteries. *Energy Storage Mater.* **2022**, *52*, 562–572.
- (14) Subramanian, K.; Alexander, G. V.; Karthik, K.; Patra, S.; Indu, M. S.; Sreejith, O. V.; Viswanathan, R.; Narayanasamy, J.; Murugan, R. A Brief Review of Recent Advances in Garnet Structured Solid Electrolyte Based Lithium Metal Batteries. *J. Energy Storage* **2021**, 33, No. 102157.
- (15) Tian, L.; Kim, J.-W.; Kim, D.-W. Solid Hybrid Electrolytes Based on Conductive Oxides and Polymer Electrolytes for All-Solid-Lithium Batteries. *Mater. Chem. Front.* **2024**, *8*, 455–484.
- (16) Chen, J.; Wu, J.; Wang, X.; Zhou, A.; Yang, Z. Research Progress and Application Prospect of Solid-State Electrolytes in Commercial Lithium-Ion Power Batteries. *Energy Storage Mater.* **2021**, 35, 70–87.
- (17) Zhu, X.; Wang, K.; Xu, Y.; Zhang, G.; Li, S.; Zhang, X.; Sun, X.; Ge, X.; Ma, Y.; Li, C. Strategies to Boost Ionic Conductivity and Interface Compatibility of Inorganic—Organic Solid Composite Electrolytes. *Energy Storage Mater.* **2021**, *36*, 291–308.
- (18) Pan, P.; Zhang, M.; Cheng, Z.; Jiang, L.; Mao, J.; Ni, C.; Chen, Q.; Zeng, Y.; Hu, Y.; Fu, K. Garnet Ceramic Fabric-Reinforced Flexible Composite Solid Electrolyte Derived from Silk Template for Safe and Long-Term Stable All-Solid-State Lithium Metal Batteries. *Energy Storage Mater.* **2022**, *47*, 279–287.
- (19) Zhao, Z.; Wu, B.; Zhang, Y.; Cui, J.; Zhang, L.; Su, Y.; Wu, F. A Promising Composite Solid Electrolyte of Garnet-Type LLZTO and Succinonitrile in Thermal Polyurethane Matrix for All-Solid-State Lithium-Ion Batteries. *Electrochem. Commun.* **2023**, *150*, No. 107472.
- (20) Tian, L. W.; Kim, J. W.; Kim, D.-W. Solid Hybrid Electrolyte Featuring a Vertically Aligned Li_{6·4}La_{3·0}Zr_{1·4}Ta_{0·6}O₁₂ Membrane for All-Solid-State Lithium Batteries. *ACS Appl. Mater. Interfaces* **2023**, *15*, 33541–33549.
- (21) Aleem, M.; Das, S.; Adelhelm, P.; Surani, P.; Khan, M. M.; Hahn, R.; Pol, V. G. Advanced Garnet-Polymer Hybrid Electrolytes

- for Enhanced Lithium Metal Battery Performance. Mater. Today Energy 2025, 49, No. 101846.
- (22) Mengesha, T. H.; Beshahwured, S. L.; Wu, S.-H.; Wu, Y.-S.; Jose, R.; Lue, S. J.; Yang, C.-C. Freestanding Trilayer Hybrid Solid Electrolyte with Electrospun Interconnected Al–LLZO Nanofibers for Solid-State Lithium-Metal Batteries. ACS Appl. Energy Mater. 2021, 4, 14554–14574.
- (23) Zhao, Y.; Yan, J.; Cai, W.; Lai, Y.; Song, J.; Yu, J.; Ding, B. Elastic and Well-Aligned Ceramic LLZO Nanofiber Based Electrolytes for Solid-State Lithium Batteries. *Energy Storage Mater.* **2019**, 23, 306–313.
- (24) La Monaca, A.; Paolella, A.; Guerfi, A.; Rosei, F.; Zaghib, K. Electrospun Ceramic Nanofibers as 1D Solid Electrolytes for Lithium Batteries. *Electrochem. Commun.* **2019**, *104*, No. 106483.
- (25) Tian, L. W.; Kim, J. W.; Hong, S.-B.; Ryu, H.-H.; Kim, U.-H.; Sun, Y.-K.; Kim, D.-W. All-solid-state lithium batteries featuring hybrid electrolytes based on ${\rm Li}^+$ ion-conductive ${\rm Li}_7{\rm La}_3{\rm Zr}_2{\rm O}_{12}$ framework and full-concentration gradient Ni-rich NCM cathode. *Chem. Eng. J.* **2022**, *450*, No. 138043.
- (26) Kim, J.-W.; Oh, M.-K.; Kim, Y.-A.; Nakate, U. T.; Kwon, E.-J.; Seo, S.; Kim, W.-K.; Ryu, K.-H.; Kim, D.-W. Enhanced Cycle Life of Lithium Metal Batteries via Modulating the Lithium-Ion Solvation Sheath with a Cross-Linked Gel Polymer Electrolyte. *J. Power Sources* **2024**, *598*, No. 234183.
- (27) Wu, C.-G.; Lu, M.-I.; Chuang, H.-J. PVdF-HFP/P123 Hybrid with Mesopores: A New Matrix for High-Conducting, Low-Leakage Porous Polymer Electrolyte. *Polymer* **2005**, *46*, 5929–5938.
- (28) Jung, Y.-C.; Kim, S.-K.; Kim, M.-S.; Lee, J.-H.; Han, M.-S.; Kim, D.-H.; Shin, W.-C.; Ue, M.; Kim, D.-W. Ceramic Separators Based on Li⁺-Conducting Inorganic Electrolyte for High-Performance Lithium-Ion Batteries with Enhanced Safety. *J. Power Sources* **2015**, 293, 675–683.
- (29) Deng, H.; He, F.; Liu, T.; Ye, M.; Wan, F.; Guo, X. Enhancing Mechanical Properties of Composite Solid Electrolyte by Ultra-High Molecular Weight Polymers. *Nanotechnology* **2024**, *35*, No. 195402.
- (30) Hevia, S. A.; Bejide, M.; Duran, B.; Rosenkranz, A.; Ruiz, H. M.; Favre, M.; del Rio, R. Nanometric Thin Films of Non-Doped Diamond-Like Carbon Grown on n-Type (P-Doped) Silicon Substrates as Electrochemical Electrodes. *J. Solid State Electrochem.* **2018**, 22, 2845–2853.
- (31) Lee, Y.-J.; Hong, S.-B.; Lee, H.-J.; Sim, H.-T.; Kim, Y.; Kim, S.; Kim, D.-W. Flexible and Thin Sulfide-Based Solid Electrolyte Sheet with Li⁺-Ion Conductive Polymer Network for All-Solid-State Lithium-Ion Batteries. *Chem. Eng. J.* **2023**, *477*, No. 146983.
- (32) Jung, Y.-C.; Lee, S.-M.; Choi, J.-H.; Jang, S. S.; Kim, D.-W. All solid-state lithium batteries assembled with hybrid solid electrolytes. *J. Electrochem. Soc.* **2015**, *162*, A704—A710.
- (33) Liu, C.; Wang, J.; Kou, W.; Yang, Z.; Zhai, P.; Liu, Y.; Wu, W.; Wang, J. A Flexible, Ion-Conducting Solid Electrolyte with Vertically Bicontinuous Transfer Channels toward High Performance All-Solid-State Lithium Batteries. *Chem. Eng. J.* **2021**, *404*, No. 126517.
- (34) Gao, H.; Huang, Y.; Zhang, Z.; Huang, J.; Li, C. Li_{6.7}La₃Zr_{1.7}Ta_{0.15}Nb_{0.15}O₁₂ Enhanced UV-Cured Poly(Ethylene Oxide)-Based Composite Gel Polymer Electrolytes for Lithium Metal Batteries. *Electrochim. Acta* **2020**, *360*, No. 137014.
- (35) Tian, L.; Kim, J.-W.; Kim, D.-W. Solid hybrid electrolytes based on conductive oxides and polymer electrolytes for all-solid-lithium batteries. *Mater. Chem. Front.* **2024**, *8*, 455–484.
- (36) Evans, J.; Vincent, C. A.; Bruce, P. G. Electrochemical Measurement of Transference Numbers in Polymer Electrolytes. *Polymer* 1987, 28, 2324–2328.
- (37) Zheng, J.; Tang, M.; Hu, Y.-Y. Lithium Ion Pathway within Li₇La₃Zr₂O₁₂–Polyethylene Oxide Composite Electrolytes. *Angew. Chem., Int. Ed.* **2016**, *55*, 12538–12542.
- (38) Chen, Y.-M.; Hsu, S.-T.; Tseng, Y.-H.; Yeh, T.-F.; Hou, S.-S.; Jan, J.-S.; Lee, Y.-L.; Teng, H. Minimization of Ion—Solvent Clusters in Gel Electrolytes Containing Graphene Oxide Quantum Dots for Lithium-Ion Batteries. *Small* **2018**, *14*, No. 1703571.

- (39) Zhai, Y.; Hou, W.; Tao, M.; Wang, Z.; Chen, Z.; Zeng, Z.; Liang, X.; Paoprasert, P.; Yang, Y.; Hu, N.; Song, S. Enabling High-Voltage "Superconcentrated Ionogel-in-Ceramic" Hybrid Electrolyte with Ultrahigh Ionic Conductivity and Single Li⁺-Ion Transference Number. *Adv. Mater.* **2022**, *34*, No. 2205560.
- (40) Lee, M. J.; Shin, D. O.; Kim, J. Y.; Oh, J.; Kang, S. H.; Kim, J.; Kim, K. M.; Lee, Y. M.; Kim, S. O.; Lee, Y.-G. Interfacial Barrier Free Organic—Inorganic Hybrid Electrolytes for Solid State Batteries. *Energy Storage Mater.* **2021**, *37*, 306—314.
- (41) Zhang, D.; Haran, B. S.; Durairajan, A.; White, R. E.; Podrazhansky, Y.; Popov, B. N. Studies on Capacity Fade of Lithium-Ion Batteries. *J. Power Sources* **2000**, *91*, 122–129.
- (42) Momma, T.; Matsunaga, M.; Mukoyama, D.; Osaka, T. AC Impedance Analysis of Lithium Ion Battery under Temperature Control. *J. Power Sources* **2012**, *216*, 304–307.
- (43) Iurilli, P.; Brivio, C.; Wood, V. On the use of electrochemical impedance spectroscopy to charaterize and model the aging phenomena of lithium-ion batteries. *J. Power Sources* **2021**, 505, No. 229860.
- (44) Jiao, X.; Rao, L.; Yap, J.; Yu, C.-Y.; Kim, J.-H. Stabilizing Cathode–Electrolyte Interphase of LiNi_{0·5}Mn_{1·5}O₄ High-Voltage Spinel by Blending Garnet Solid Electrolyte in Lithium-Ion Batteries. *J. Power Sources* **2023**, *561*, No. 232748.
- (45) Kim, K.; Ma, H.; Park, S.; Choi, N.-S. Electrolyte-Additive-Driven Interfacial Engineering for High-Capacity Electrodes in Lithium-Ion Batteries: Promise and Challenges. *ACS Energy Lett.* **2020**, *5*, 1537–1553.
- (46) Park, C.; Lee, E.; Kim, S. H.; Han, J. G.; Hwang, C.; Joo, S. H.; Baek, K.; Kang, S. J.; Kwak, S. K.; Song, H. K.; Choi, N. S. Malonic-Acid-Functionalized Fullerene Enables the Interfacial Stabilization of Ni-Rich Cathodes in Lithium-Ion Batteries. *J. Power Sources* **2022**, *521*, No. 230923.
- (47) Wang, X.; Song, Z.; Wu, H.; Yu, H.; Feng, W.; Armand, M.; Huang, X.; Zhou, Z.; Zhang, H. Anion Donicity of Liquid Electrolytes for Lithium Carbon Fluoride Batteries. *Angew. Chem., Int. Ed.* **2022**, *61*, No. e202211623.
- (48) Ma, H.; Hwang, D.; Ahn, Y. J.; Lee, M.-Y.; Kim, S.; Lee, Y.; Lee, S.-M.; Kwak, S. K.; Choi, N.-S. In Situ Interfacial Tuning To Obtain High-Performance Nickel-Rich Cathodes in Lithium Metal Batteries. ACS Appl. Mater. Interfaces 2020, 12, 29365—29375.
- (49) Deng, T.; Fan, X.; Cao, L.; Chen, J.; Hou, S.; Ji, X.; Chen, L.; Li, S.; Zhou, X.; Hu, E.; Su, D.; Yang, X.-Q.; Wang, C. Designing In-Situ-Formed Interphases Enables Highly Reversible Cobalt-Free LiNiO₂ Cathode for Li-Ion and Li-Metal Batteries. *Joule* **2019**, 3, 2550–2564.

